

Emerging Multidimensional Real-Space Topological Structures at Chiral Bound States in the Continuum

Xingqi Zhao¹, Jingguang Chen¹, Jiajun Wang^{1,5,*}, Lixi Rao¹, Wenzhe Liu^{1,2,5}, Fang Guan^{1,2,5}, C. T. Chan³, Lei Shi^{1,2,4,5,†} and Jian Zi^{1,2,4,5,‡}

¹*State Key Laboratory of Surface Physics, Key Laboratory of Micro- and Nano-Photonic Structures (Ministry of Education) and Department of Physics, Fudan University, Shanghai 200433, China*

²*Institute for Nanoelectronic devices and Quantum computing, Fudan University, Shanghai 200438, China*

³*Department of Physics, The Hong Kong University of Science and Technology, Clear Water Bay, Hong Kong, 999077, China*

⁴*Collaborative Innovation Center of Advanced Microstructures, Nanjing University, Nanjing 210093, China and*

⁵*Shanghai Research Center for Quantum Sciences, Shanghai 201315, China*

As widely studied topological singularities, bound states in the continuum (BICs) have revealed rich physical properties through their momentum-space topology. Here, we reveal and experimentally demonstrate that magnetically induced chiral BICs possess multidimensional topological structures extending into real space. We design and realize a gyromagnetic photonic crystal slab where magnetic field breaks the time-reversal symmetry and lifts the degeneracy of BICs, creating a pair of chiral BICs with opposite circular polarizations. Near-field scanning measurements reveal phase vortices with quantized topological charges, spatially distributed near-field chirality, and skyrmionic Stokes textures arising from magnetic control. Our work unveils a previously unexplored dimension of BIC topology and establishes gyromagnetic photonic crystals as versatile platforms for manipulating complex topological states.

Topological structures - from phase vortices [1, 2] and topological defects [3] to more exotic configurations like skyrmions [4, 5] - appear across various physical systems and exhibit distinct topological properties. These structures not only provide frameworks for understanding physical phenomena but also exhibit rich physical effects themselves [6–9]. For instance, magnetic flux quantization in superconductors are connected with topological vortices [6]; in classical wave systems, vortex fields can govern energy flow and create localized field enhancement [10, 11]. The rich physics and effects of topological structures have motivated their exploration across various research fields.

In modern photonics and optics, the explorations of topological structures have proven particularly fruitful. These singular optical fields, manifesting in various forms from structured polarization configurations to phase vortices and optical skyrmions [1, 5, 12–14], provide powerful capabilities and new degrees of freedom in light manipulation [15–17], communications [18, 19], information processing [20, 21], sensing [22], and light-matter interaction [2, 23]. To explore and harness these topological optical fields, various optical platforms have been developed. Among them, engineered photonic structures like photonic crystals (PhCs) have created a diverse landscape of topological physics [24, 25]. The interaction between light and periodic structures provides a versatile platform for exploring photonic topological structures in multiple dimensions, leading to interesting discoveries and realizations such as topological valleys [26], Dirac vortex [27], vortex beam [28], and spatiotemporal vortex [29].

Bound states in the continuum (BICs), emerging as topological singularities in momentum space, represent a particularly intriguing class of topological states in PhC

slabs [30–33]. Studies have established that BICs exhibit rich topological characteristics: they carry polarization vortices in momentum space, which can lead to the generation of vectorial beams, phase vortices, and even skyrmionic textures [28, 34–36]. To date, BICs are primarily explored by their momentum-space topology [37–40], even though real-space electromagnetic field distributions fundamentally reflect elaborate characteristics of these singular states and directly mediate light-matter interactions. The real-space topological nature of BICs, such as the spatial topological configurations of electromagnetic fields, remains largely unexplored. Recent theoretical advances have revealed the emergence of phase vortices in the near-field distribution of chiral BICs [41], suggesting that momentum-space topology connects unexplored real-space field configurations. It inspires a broad landscape for exploring multidimensional topological structures across momentum and real space through BICs, opening new avenues in topological photonics.

In this work, we reveal multidimensional real-space topological structures in magnetically induced chiral BICs. By applying an magnetic field to a gyromagnetic PhC slab composed of yttrium iron garnet (YIG) cylinders, we transform doubly degenerate BICs into a pair of chiral BICs with opposite handedness in the far field. Through near-field measurements, we uncover that these chiral BICs host multidimensional real-space topological structures: phase vortices, spatially distributed near-field chirality patterns, and skyrmionic Stokes textures. All these topological structures can be switched by reversing the magnetic field. Our findings establish a new paradigm connecting momentum-space and real-space topology in BICs and open new avenues for magnetically tunable topological structures.

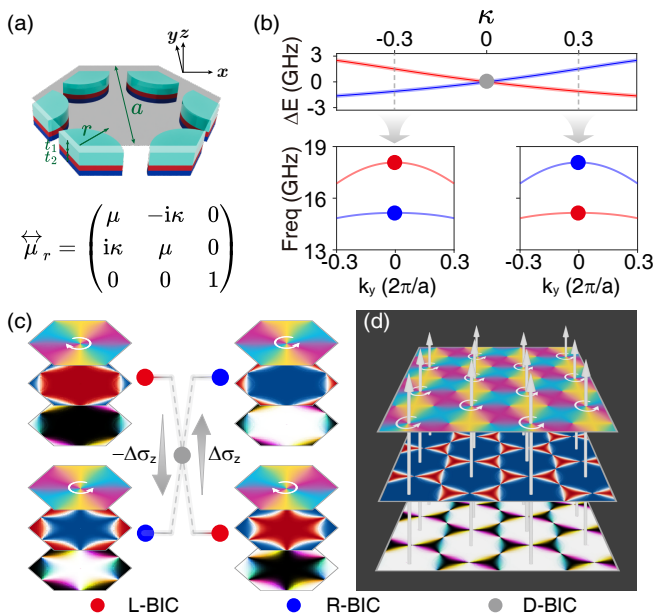


FIG. 1. (a) Upper panel: a unit cell of the PhC slab, where the gray plane indicates where the near-field distributions are evaluated in later discussions. Lower panel: the relative permeability tensor $\overleftrightarrow{\mu}_r$ of YIG. (b) Top: evolution of the BICs with κ . Bottom: representative photonic band structures for $\kappa = \pm 0.3$. Red/blue/gray dots denote L-BIC/R-BIC/D-BIC, respectively. (c) Real-space topological textures in a unit cell associated with the chiral BICs, evaluated at the gray plane shown in (a). From top to bottom: (i) phase distributions, (ii) chirality distributions, and (iii) Stokes vector distributions. Reversing the magnetic field swaps the two chiral BICs and their associated topological textures. (d) Schematic real-space topological structures of the R-BIC across the PhC slab.

Figure 1(a) shows the schematic view of a unit cell of the gyromagnetic PhC slab, which comprises a honeycomb lattice of YIG cylinders. Here, the radius r and thickness t_1 of the YIG cylinder are 3 mm and 1.4 mm, respectively. The lattice constant a is 14 mm. In the absence of a magnetic field, the structure supports a pair of doubly degenerate BICs (D-BICs) at the Γ point. When the YIG cylinders are magnetized by permanent magnets placed beneath the slab, where the magnets have the thickness $t_2 = 1$ mm and the same radius r , the YIG exhibits a gyromagnetic response described by the relative permeability tensor [42]

$$\overleftrightarrow{\mu}_r = \begin{pmatrix} \mu & -i\kappa & 0 \\ i\kappa & \mu & 0 \\ 0 & 0 & 1 \end{pmatrix}. \quad (1)$$

The off-diagonal element κ is controlled by the out-of-plane magnetic field. With this magnetic field, the degeneracy is lifted. At the Γ point, the coupled-mode dynamics can be captured by the effective Hamiltonian [43]:

$$\mathbf{H} = E_0 + \Delta\sigma_z. \quad (2)$$

Here E_0 is the energy of the degenerate pair, and Δ is the Zeeman term which is governed by the magnetic field (the value of κ), controlling the splitting of modes. As shown in the upper panel of Fig. 1(b), increasing $|\kappa|$ continuously separates the eigenfrequencies of modes with an energy gap ΔE , and two chiral BICs emerge from the original D-BICs. Two chiral BICs carry opposite handedness: In the vicinity of them, the radiative channels exhibit circular polarization in far field, one corresponds to left-hand circular polarization (L-BIC) and the other to right-hand circular polarization (R-BIC) [41]. Flipping the magnetic field flips the sign of κ and swaps the handedness of the two branches, as shown in Fig. 1(b).

The topology of BICs is typically characterized in momentum space through far-field radiation properties [32, 33]. Here, we reveal that these chiral BICs exhibit unprecedented richness in real-space topology, manifested in their near-field distributions. Figure 1(c) exhibits the near-field topological structures in a unit cell for the paired chiral BICs under the two opposite magnetization directions described in Fig. 1(b), showing topological characteristics that extend beyond the conventional far-field properties of BICs. The six-fold rotational (C_6) symmetry of the structure enforces a phase vortex at the unit cell center. From group theory, the paired chiral BICs correspond to the E_{2a} and E_{2b} representations of the C_6 point group, which require the complex field to acquire a winding phase of $\pm 4\pi$ around the rotation center for the R-BIC (L-BIC). This phase vortex is accompanied by spatially distributed chirality in the near field. The near field chirality is made explicit by the Stokes parameter S_3/S_0 , with $S_3 > 0$ corresponds to right-handed circularly polarized (RCP) and $S_3 < 0$ corresponds to left-handed circularly polarized (LCP). There is a pronounced difference of chirality between the vicinity of the YIG region and the surrounding areas, revealing a strongly localized contrast. When considering the full Stokes vector field, it reveals that the polarization further organizes into a topological skyrmionic texture in real space. Note that, upon reversing the magnetization, all these topological structures reverse accordingly. When considering the whole PhC slabs (Fig. 1(d)), they form a coherent periodic pattern, highlighting that the topological characteristics of chiral BICs extend beyond momentum space to robust real-space configurations.

To experimentally realize the chiral BICs, we fabricated the designed PhC slab, with a photo shown in Fig. 2(a). Each YIG pillar is mounted on a magnet, and the YIG-magnet units are embedded in a foam slab perforated with a honeycomb lattice, as shown in the right panel. With the external magnetic field, two bands carry opposite signs of the S_3 in far field, indicating opposite handedness of their radiation. The calculated band structures are provided in the Supplemental Material Sec. 2.

The opposite chirality leads to distinct transmission responses under circularly polarized incidence. Figure

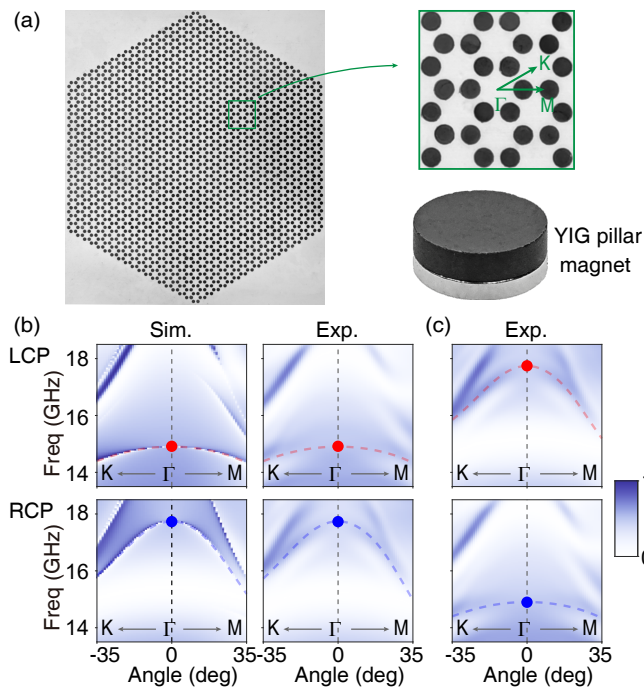


FIG. 2. (a) Photo of the experimental sample. (b) Simulated and measured co-polarized transmission spectra under circularly polarized incidence for the sample magnetized in the positive B direction. Upper row: LCP incidence; Lower row: RCP incidence. Dashed curves mark bands whose handedness matches that of the incident light. (c) Measured co-polarized transmission spectra under reversed magnetization.

2(b) presents the co-polarized transmission spectra for positive B, where the magnetic field is defined as positive when the north pole of the magnets upward. In this configuration, modes in the lower band radiate predominantly LCP, and those in the upper band radiate predominantly RCP. Consequently, near Γ point, LCP incidence selectively excites the lower band (traced by the red dashed curve), whereas the upper band is not efficiently excited and thus barely visible in the spectrum. Under RCP incidence, the upper band is excited (blue dashed curve) while the lower band becomes inconspicuous for the same reason. Note that the Γ points of the two bands correspond to BICs, which cannot be excited by any external incidence and thus do not appear in the transmission spectra for either polarization. When reversing the magnetic field, the chiral responses swap (Fig. 2(c)). These transmission measurements directly demonstrate the realization of chiral BICs from the far field, and characterize their magnetically controllable chiral responses with the far-field incidence.

We then characterize the near-field properties of the chiral BICs. Figure 3(a) shows a schematic of the near-field scanning setup: a probe scans above the PhC surface to map the spatial distribution of the electric field. Two types of probes are used for the measurement of normal

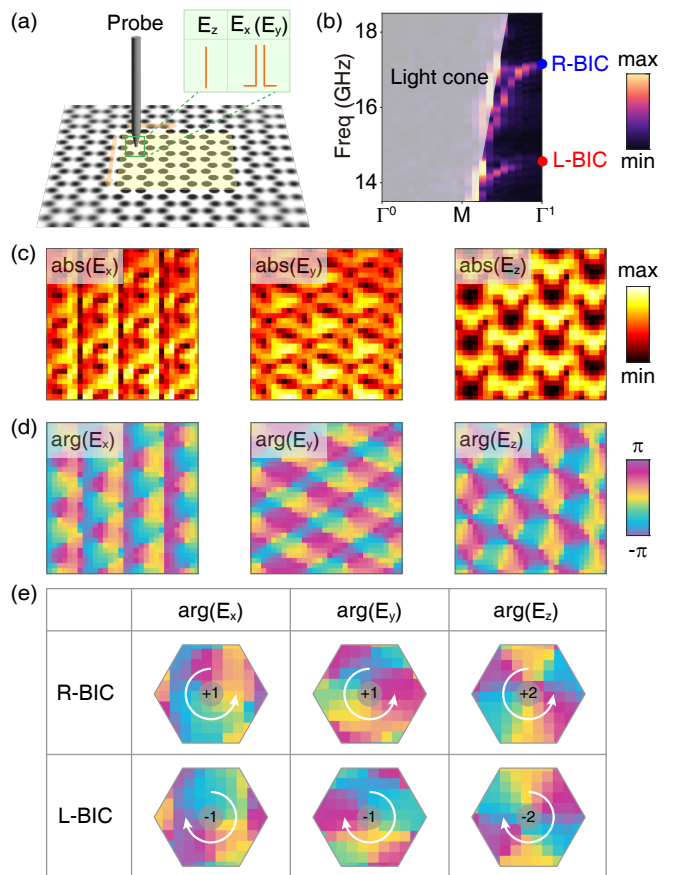


FIG. 3. (a) Schematic view of the near-field scanning setup. (b) The measured near-field Fourier components of the E_z amplitude, showing the two bands of interest. The gray region denotes the light cone. (c)-(d) Measured amplitude (c) and phase (d) of the electric field for the R-BIC. (e) The phase vortices in the unit cell for the R-BIC and L-BIC, where the L-BIC has opposite phase winding compared to the R-BIC.

electric field (E_z) and tangential electric field (E_x and E_y). Here, the measured Fourier spectrum of the E_z component (Fig. 3(b)) reveals the two bands of interest. By selecting Fourier components in the vicinity of the chiral BICs and performing inverse Fourier transform, we can extract the real-space near-field distribution of chiral BICs. Details of the experimental setup and data analyze are discussed in Supplemental Material Sec. 7.

Figures 3(c) and 3(d) present the measured amplitude and phase distributions of the electric field for the R-BIC. Notably, all field components vanish at the unit-cell center, manifesting as zero-intensity points. The phase distributions reveal that these zero-amplitude points are phase singularities: the phase winds continuously around the center, forming vortices in real space. The topological charge q of these phase vortices is defined as [30]

$$q = \frac{1}{2\pi} \oint_C d\mathbf{r} \cdot \nabla \phi(\mathbf{r}), \quad (3)$$

where ϕ is the phase, \mathbf{r} is the spatial coordinate, and the

integration is performed along a closed loop C around the singularity. Figure 3(e) summarizes the topological phase structures in a unit cell. For the R-BIC, all field components (E_x, E_y, E_z) exhibit counterclockwise phase winding around the center, with E_x and E_y carrying a topological charge of $q = +1$, and E_z carrying $q = +2$. In contrast, the L-BIC exhibits opposite phase winding in all components. This reversal of vortex winding between the paired chiral BICs demonstrates that the photonic pseudospin (corresponding to chirality) is intrinsically locked to the orbital angular momentum (corresponding to the phase vortices) in this system [41].

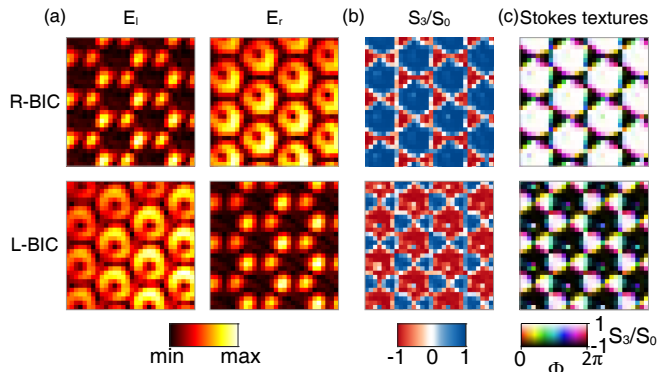


FIG. 4. (a) The left-handed circular (left panel) and right-handed circular (right panel) components of the near-field electric field of chiral BICs. (b) The normalized third Stokes parameter (S_3/S_0) of chiral BICs in the near field. (c) The distribution of Stokes vectors, showing skyrmionic textures. From top to bottom: measured results of R-BIC and L-BIC.

We further investigate the near-field chirality of the chiral BICs. In Fig. 4(a), we provide the left-handed and right-handed circular components (E_l and E_r) of the electric field, which are defined by

$$E_{l(r)} = E_x \pm iE_y. \quad (4)$$

For each BIC, the near field exhibits a distinct chirality distribution: For the R-BIC, the E_l component is mainly localized around the YIG cylinders, while the E_r component is mainly localized in other regions. Note that the center of the unit cell is a singularity with zero amplitude for both E_l and E_r . This spatially separated chirality distribution reveals that the magnetic field not only induces far-field chirality in the radiation, but also creates unique chiral textures in the near field, with opposite circular polarizations confined to distinct spatial regions. The L-BIC shows the opposite pattern, with E_l and E_r distributions reversed compared to the R-BIC. This chirality distribution is quantitatively captured by the normalized third Stokes parameter S_3/S_0 , which measures the degree of circular polarization. As shown in Fig. 4(b), the S_3/S_0 map reveals strong spatial variation. For the R-BIC, negative values are concentrated around the YIG

cylinders and positive values in other regions, confirming the spatially segregated chirality distribution observed in Fig. 4(a). For the L-BIC, the sign distribution of S_3/S_0 is reversed. Note that the near-field chirality here is characterized by the circular polarization of the in-plane electric field [14, 44–46], which differs from the optical chirality density involving both electric and magnetic fields [14].

Nontrivial topological distributions in vector fields represent fundamental properties with inherent stability, exemplified by skyrmionic textures, which have recently garnered considerable interest across diverse physical systems [4, 5, 8, 47–50]. Here we reveal that similar topological textures also appear in the real-space near-field distribution for chiral BICs. Considering the full normalized Stokes vector $\mathbf{S} = (S_1, S_2, S_3)/S_0$ of the chiral BIC, we observe skyrmionic organization in real space, as shown in Fig. 4(c). Two key features characterize these textures: (1) the S_3 component changes sign from the center to the boundary of the unit cell, representing a transition from one circular polarization to the opposite; (2) the azimuthal angle $\Phi = \arg(S_1 + iS_2)$ winds continuously around the center. Notably, the paired R-BIC and L-BIC exhibit opposite signs of S_3 while maintaining the same winding direction of Φ . These real-space near-field Stokes textures demonstrate that complex topological structures are also intrinsic properties of optical modes in PhC slabs, embodying rich polarization configurations in the confined electromagnetic fields.

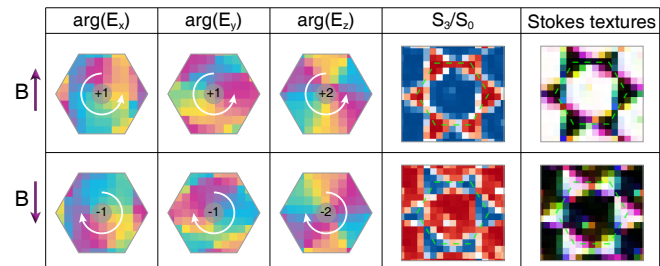


FIG. 5. Upon reversing the magnetic field, the BIC on the upper band transforms from R-BIC to L-BIC, with its near-field topological structures switching correspondingly.

The real-space topological structures are governed by the direction of the magnetic field. To experimentally verify and demonstrate the magnetic control, we fabricated another sample with the magnets oriented oppositely. This reverses the magnetic field, flips the sign of κ , and swaps the handedness of the two chiral BICs. The upper band, which supports an R-BIC in the first sample, now hosts an L-BIC; conversely, the lower band switches from L-BIC to R-BIC.

Figure 5 compares the measured near-field topological structures of the upper-band BIC for both magnetization directions. Under upward magnetization (top row), the BIC exhibits counterclockwise phase winding in all the electric field components, negative S_3 in the YIG re-

gions, and corresponding Stokes vector textures. Upon reversing the magnetic field (bottom row), all these topological features reverse: the phase vortices wind clockwise, the chirality distribution inverts, and the Stokes textures flip accordingly. These experimental results confirm that the real-space topological structures are intimately linked with the chiral BICs and can be deterministically switched by the magnetic field direction.

In conclusion, our work unveils rich real-space topological structures at chiral BICs beyond conventional momentum-space characterizations. Applying an external magnetic field to a gyromagnetic PhC slab not only creates chiral BICs with opposite handedness in the far field but also generates multidimensional real-space topological structures in the near field, including phase vortices, spatially distributed chirality, and skyrmionic Stokes textures. These topological structures can enhance nonlinear processes and sensing through chiral field localization, and create new paradigms for chiral light-matter interactions and topological phase engineering. This magnetic control of real-space topological structures establishes a new paradigm for topological photonics, enabling on-demand manipulation of topological states. Future directions include exploring magnetic field control of other topological singularities beyond degenerate BICs, investigating additional topological invariants in these systems, and studying other topological structures. These investigations may reveal new topological phenomena and advance our fundamental understanding of multidimensional topology in photonic systems.

This work is supported by National Key R&D Program of China (No. 2023YFA1406900, No. 2022YFA1404800, and No. 2021YFA1400603); National Natural Science Foundation of China (No. 12404427, No. 12234007, No. 124B2084, No. 12321161645, No. 12221004, No. 125B2087, No. T2394480, and No. T2394481); Science and Technology Commission of Shanghai Municipality (No. 24YF2702400, No. 2019SHZDZX01, No. 23DZ2260100, and No. 24142200100); Research Grants Council (RGC) of Hong Kong (CRS_HKUST601/23).

X.Z., J.C. and J.W. contributed equally to this Letter.

* jiajunwang@fudan.edu.cn

† lshi@fudan.edu.cn

‡ jzi@fudan.edu.cn

- [1] G. J. Gbur, *Singular optics* (CRC press, 2016).
- [2] G. F. Quinteiro Rosen, P. I. Tamborenea, and T. Kuhn, Interplay between optical vortices and condensed matter, *Reviews of Modern Physics* **94**, 035003 (2022).
- [3] N. D. Mermin, The topological theory of defects in ordered media, *Reviews of Modern Physics* **51**, 591 (1979).
- [4] N. Nagaosa and Y. Tokura, Topological properties and dynamics of magnetic skyrmions, *Nature Nanotechnology* **8**, 899 (2013).
- [5] Y. Shen, Q. Zhang, P. Shi, L. Du, X. Yuan, and A. V. Zayats, Optical skyrmions and other topological quasiparticles of light, *Nature Photonics* **18**, 15 (2024).
- [6] G. Blatter, M. V. Feigel'man, V. B. Geshkenbein, A. I. Larkin, and V. M. Vinokur, Vortices in high-temperature superconductors, *Reviews of Modern Physics* **66**, 1125 (1994).
- [7] J. R. Abo-Shaeer, C. Raman, J. M. Vogels, and W. Ketterle, Observation of vortex lattices in Bose-Einstein condensates, *Science* **292**, 476 (2001).
- [8] A. Fert, N. Reyren, and V. Cros, Magnetic skyrmions: advances in physics and potential applications, *Nature Reviews Materials* **2**, 1 (2017).
- [9] J. Ni, C. Huang, L.-M. Zhou, M. Gu, Q. Song, Y. Kivshar, and C.-W. Qiu, Multidimensional phase singularities in nanophotonics, *Science* **374**, eabj0039 (2021).
- [10] B. Wang, Z. Che, C. Cheng, C. Tong, L. Shi, Y. Shen, K. Y. Bliokh, and J. Zi, Topological water-wave structures manipulating particles, *Nature*, 1 (2025).
- [11] S. Zhao, Z. Tian, C. Shen, S. Yang, J. Xia, T. Li, Z. Xie, P. Zhang, L. P. Lee, S. A. Cummer, *et al.*, Topological acoustofluidics, *Nature Materials*, 1 (2025).
- [12] Q. Zhan, Cylindrical vector beams: from mathematical concepts to applications, *Advances in Optics and Photonics* **1**, 1 (2009).
- [13] C. He, Y. Shen, and A. Forbes, Towards higher-dimensional structured light, *Light: Science & Applications* **11**, 205 (2022).
- [14] Y. Chen, W. Du, Q. Zhang, O. Ávalos-Ovando, J. Wu, Q.-H. Xu, N. Liu, H. Okamoto, A. O. Govorov, Q. Xiong, *et al.*, Multidimensional nanoscopic chiroptics, *Nature Reviews Physics* **4**, 113 (2022).
- [15] D. Kleckner and W. T. Irvine, Creation and dynamics of knotted vortices, *Nature Physics* **9**, 253 (2013).
- [16] T. Bauer, P. Banzer, E. Karimi, S. Orlov, A. Rubano, L. Marrucci, E. Santamato, R. W. Boyd, and G. Leuchs, Observation of optical polarization Möbius strips, *Science* **347**, 964 (2015).
- [17] Z. Hu, D. Bongiovanni, Z. Wang, X. Wang, D. Song, J. Xu, R. Morandotti, H. Buljan, and Z. Chen, Topological orbital angular momentum extraction and twofold protection of vortex transport, *Nature Photonics* **19**, 162 (2025).
- [18] A. E. Willner, H. Huang, Y. Yan, Y. Ren, N. Ahmed, G. Xie, C. Bao, L. Li, Y. Cao, Z. Zhao, *et al.*, Optical communications using orbital angular momentum beams, *Advances in Optics and Photonics* **7**, 66 (2015).
- [19] A. E. Willner, K. Pang, H. Song, K. Zou, and H. Zhou, Orbital angular momentum of light for communications, *Applied Physics Reviews* **8** (2021).
- [20] N. Bozinovic, Y. Yue, Y. Ren, M. Tur, P. Kristensen, H. Huang, A. E. Willner, and S. Ramachandran, Terabit-scale orbital angular momentum mode division multiplexing in fibers, *Science* **340**, 1545 (2013).
- [21] B. Ndagano, B. Perez-Garcia, F. S. Roux, M. McLaren, C. Rosales-Guzman, Y. Zhang, O. Mouane, R. I. Hernandez-Aranda, T. Konrad, and A. Forbes, Characterizing quantum channels with non-separable states of classical light, *Nature Physics* **13**, 397 (2017).
- [22] M. P. Lavery, F. C. Speirits, S. M. Barnett, and M. J.

- Padgett, Detection of a spinning object using light's orbital angular momentum, *Science* **341**, 537 (2013).
- [23] H. He, M. Friese, N. Heckenberg, and H. Rubinsztein-Dunlop, Direct observation of transfer of angular momentum to absorptive particles from a laser beam with a phase singularity, *Physical Review Letters* **75**, 826 (1995).
- [24] L. Lu, J. D. Joannopoulos, and M. Soljačić, Topological photonics, *Nature Photonics* **8**, 821 (2014).
- [25] T. Ozawa, H. M. Price, A. Amo, N. Goldman, M. Hafezi, L. Lu, M. C. Rechtsman, D. Schuster, J. Simon, O. Zilberberg, *et al.*, Topological photonics, *Reviews of Modern Physics* **91**, 015006 (2019).
- [26] J.-W. Dong, X.-D. Chen, H. Zhu, Y. Wang, and X. Zhang, Valley photonic crystals for control of spin and topology, *Nature Materials* **16**, 298 (2017).
- [27] X. Gao, L. Yang, H. Lin, L. Zhang, J. Li, F. Bo, Z. Wang, and L. Lu, Dirac-vortex topological cavities, *Nature Nanotechnology* **15**, 1012 (2020).
- [28] B. Wang, W. Liu, M. Zhao, J. Wang, Y. Zhang, A. Chen, F. Guan, X. Liu, L. Shi, and J. Zi, Generating optical vortex beams by momentum-space polarization vortices centred at bound states in the continuum, *Nature Photonics* **14**, 623 (2020).
- [29] R.-Y. Zhang, X. Cui, Y.-S. Zeng, J. Chen, W. Liu, M. Wang, D. Wang, Z.-Q. Zhang, N. Wang, G.-B. Wu, *et al.*, Bulk–spatiotemporal vortex correspondence in gyromagnetic zero-index media, *Nature*, 1 (2025).
- [30] C. W. Hsu, B. Zhen, A. D. Stone, J. D. Joannopoulos, and M. Soljačić, Bound states in the continuum, *Nature Reviews Materials* **1**, 1 (2016).
- [31] L. Huang, L. Xu, D. A. Powell, W. J. Padilla, and A. E. Miroshnichenko, Resonant leaky modes in all-dielectric metasystems: Fundamentals and applications, *Physics Reports* **1008**, 1 (2023).
- [32] M. Kang, T. Liu, C. Chan, and M. Xiao, Applications of bound states in the continuum in photonics, *Nature Reviews Physics* **5**, 659 (2023).
- [33] J. Wang, P. Li, X. Zhao, Z. Qian, X. Wang, F. Wang, X. Zhou, D. Han, C. Peng, L. Shi, *et al.*, Optical bound states in the continuum in periodic structures: mechanisms, effects, and applications, *Photonics Insights* **3**, R01 (2024).
- [34] C. Huang, C. Zhang, S. Xiao, Y. Wang, Y. Fan, Y. Liu, N. Zhang, G. Qu, H. Ji, J. Han, *et al.*, Ultrafast control of vortex microlasers, *Science* **367**, 1018 (2020).
- [35] J. Wang, X. Wang, Z. Wu, X. Zhao, S. Wu, L. Shi, Y. Kivshar, and J. Zi, Inherent spin-orbit locking in topological lasing via bound state in the continuum, *Physical Review Letters* **134**, 133802 (2025).
- [36] L. Rao, J. Wang, X. Wang, S. Wu, X. Zhao, W. Liu, R. Xie, Y. Shen, L. Shi, and J. Zi, Meron spin textures in momentum space spawning from bound states in the continuum, *Physical Review Letters* **135**, 026203 (2025).
- [37] B. Zhen, C. W. Hsu, L. Lu, A. D. Stone, and M. Soljačić, Topological nature of optical bound states in the continuum, *Physical Review Letters* **113**, 257401 (2014).
- [38] Y. Zhang, A. Chen, W. Liu, C. W. Hsu, B. Wang, F. Guan, X. Liu, L. Shi, L. Lu, and J. Zi, Observation of polarization vortices in momentum space, *Physical Review Letters* **120**, 186103 (2018).
- [39] H. M. Doeleman, F. Monticone, W. den Hollander, A. Alù, and A. F. Koenderink, Experimental observation of a polarization vortex at an optical bound state in the continuum, *Nature Photonics* **12**, 397 (2018).
- [40] W. Liu, B. Wang, Y. Zhang, J. Wang, M. Zhao, F. Guan, X. Liu, L. Shi, and J. Zi, Circularly polarized states spawning from bound states in the continuum, *Physical Review Letters* **123**, 116104 (2019).
- [41] X. Zhao, J. Wang, W. Liu, Z. Che, X. Wang, C. Chan, L. Shi, and J. Zi, Spin-orbit-locking chiral bound states in the continuum, *Physical Review Letters* **133**, 036201 (2024).
- [42] D. M. Pozar, *Microwave Engineering: Theory and Techniques* (John Wiley & sons, 2021).
- [43] Z. Wang and S. Fan, Magneto-optical defects in two-dimensional photonic crystals, *Applied Physics B* **81**, 369 (2005).
- [44] P. Lodahl, S. Mahmoodian, S. Stobbe, A. Rauschenbeutel, P. Schneeweiss, J. Volz, H. Pichler, and P. Zoller, Chiral quantum optics, *Nature* **541**, 473 (2017).
- [45] I. Söllner, S. Mahmoodian, S. L. Hansen, L. Midolo, A. Javadi, G. Kiršanskė, T. Pregnolato, H. El-Ella, E. H. Lee, J. D. Song, *et al.*, Deterministic photon–emitter coupling in chiral photonic circuits, *Nature Nanotechnology* **10**, 775 (2015).
- [46] R. Shreiner, K. Hao, A. Butcher, and A. A. High, Electrically controllable chirality in a nanophotonic interface with a two-dimensional semiconductor, *Nature Photonics* **16**, 330 (2022).
- [47] U. I. Kara, B. Chen, S. Čopar, S. Li, R. Mamtani, Y. Xu, A. H. Weible, E. C. Boerner, Z. Yang, Y. Yao, R. L. B. Selinger, U. Tkalec, and X. Wang, Multistable polar textures in geometrically frustrated nematic liquid crystals, *Nature Physics* **21**, 1404 (2025).
- [48] J. Ma, J. Yang, S. Liu, B. Chen, X. Li, C. Song, G. Qiu, K. Zou, X. Hu, F. Li, Y. Yu, and J. Liu, Nanophotonic quantum skyrmions enabled by semiconductor cavity quantum electrodynamics, *Nature Physics* **21**, 1462 (2025).
- [49] S. Huh, W. Yun, G. Yun, S. Hwang, K. Kwon, J. Hur, S. Lee, H. Takeuchi, S. K. Kim, and J.-y. Choi, Stable singular fractional skyrmion spin texture from the quantum Kelvin–Helmholtz instability, *Nature Physics* **21**, 1398 (2025).
- [50] J. Schwab, A. Neuhaus, P. Dreher, S. Tsesses, K. Cohen, F. Mangold, A. Mantha, B. Frank, G. Bartal, F.-J. Meyer zu Heringdorf, T. J. Davis, and H. Giessen, Skyrmion bags of light in plasmonic Moiré superlattices, *Nature Physics* **21**, 988 (2025).